Detailed diagnostics of an X-ray flare in the single giant HR 9024

Paola Testa[1], Fabio Reale[2,3], David Garcia-Alvarez[4], David P. Huenemoerder[1]

ABSTRACT

We analyze a 96 ks *Chandra* HETGS observation of the single G-type giant HR 9024. The high flux allows us to examine spectral line and continuum diagnostics at high temporal resolution, to derive plasma parameters. A time-dependent 1D hydrodynamic model of a loop with half-length $L = 5 \times 10^{11}$ cm ($\sim R_\star/2$), cross-section radius $r = 4.3 \times 10^{10}$ cm, with a heat pulse of 15 ks and 2×10^{11} erg cm^{-2} s^{-1} deposited at the loop footpoints, satisfactorily reproduces the observed evolution of temperature and emission measure, derived from the analysis of the strong continuum emission. For the first time we can compare predictions from the hydrodynamic model with single spectral features, other than with global spectral properties. We find that the model closely matches the observed line emission, especially for the hot ($\sim 10^8$ K) plasma emission of the Fe XXV complex at ~ 1.85Å.

The model loop has $L/R_\star \sim 1/2$ and aspect ratio $r/L \sim 0.1$ as typically derived for flares observed in active stellar coronae, suggesting that the underlying physics is the same for these very dynamic and extreme phenomena in stellar coronae independently on stellar parameters and evolutionary stage.

1. Introduction

The first X-ray stellar surveys showed widespread presence of coronal emission in the cool half of the H-R diagram (see e.g., Vaiana et al. 1981 for a review). Improved spatial and spectral resolution have provided us with more powerful tools for investigating the characteristics of the X-ray coronal activity in late-type stars, and for exploring the underlying processes at work in stars with different stellar parameters, and evolutionary stage.

[1]Massachusetts Institute of Technology, Kavli Institute for Astrophysics and Space Research, 70 Vassar street, Cambridge, MA 02139, USA; testa@space.mit.edu

[2]Dipartimento di Scienze Fisiche & Astronomiche, Sezione di Astronomia, Università di Palermo Piazza del Parlamento 1, 90134 Palermo, Italy

[3]INAF - Osservatorio Astronomico di Palermo, Piazza del Parlamento 1, 90134 Palermo, Italy

[4]Imperial College London, Blackett Laboratory, Prince Consort Rd, London, SW7 2AZ, UK

X-ray observations of late-type stars show that coronal phenomena observed at close range on the Sun are common in late-type stars though they occur on more extreme scales in very active stars. For instance, stars at higher activity levels have reach much higher temperatures and densities (e.g., Sanz-Forcada et al. 2002; Testa et al. 2004; Ness et al. 2004) than typically observed for solar coronal plasma. Analogously, coronal flares are routinely observed in late-type stars with characteristics similar to those observed in solar flares, e.g., fast rise and slow decay (e.g., Reale 2002 for a review), but at the same time the flare frequency and intensity can be dramatically larger than observed on the Sun, with stellar X-ray luminosity increasing orders of magnitude with respect to the quiescent level (e.g., Favata et al. 2000; Osten et al. 2006).

The analysis of lightcurves during flares provides us with insights into the characteristics of the coronal structures and therefore of the magnetic field (e.g., Schmitt & Favata 1999; Favata et al. 2000; Reale et al. 2004). Even though stellar flares are spatially unresolved, a great deal of information on the coronal heating and on the plasma structure morphology can be inferred from the detailed modeling of stellar flares; for instance, if enough data statistics is available for moderately time-resolved spectral analysis, the study of the complete evolution of a flare allows to infer whether the flare occurs in closed coronal structures (loops), what is the size of these flaring structures, whether continuous heating is present throughout the flare, and even constraints on the location and distribution of the heating (see Reale et al. 2004, and §4.2 for a detailed discussion).

This work presents a detailed modeling of a large X-ray flare on the single evolved G1 III giant HR 9024, observed with the *Chandra* High Energy Transmission Grating. Most of the flare is observed, from the rise phase to the late decay, allowing to constrain a detailed hydrodynamic simulation of the flaring structure. The analysis of this flare is especially interesting in the context of X-ray activity of evolved giants. HR 9024 is an intermediate mass star ($M_\star \sim 2.9 M_\odot$) in the Hertzsprung gap, that is in its initial rapid (< 1 Myr) phase of post-main sequence evolution when it enters the cool region of the H-R diagram, and it develops a subphotospheric convective layer (see e.g., Pizzolato et al. 2000). The intermediate mass Hertzsprung gap giants are strong X-ray emitters ($L_{\rm X} \sim 10^{31}$ erg s^{-1}) while their main-sequence progenitors, late-B or early-A type, are X-ray dark lacking the fundamental ingredients to sustain X-ray activity, either magnetic-dynamo as in late-type stars or strong winds as in massive stars. The onset of an efficient convective layer, together with their typically fast rotation rates (due to the little if any loss of angular momentum in their main sequence phase) is thought to generate a dynamo mechanism sustaining the X-ray activity of these evolved yellow giants. The young coronae of these stars are characterized by high temperature and density (e.g., Ayres et al. 1998; Testa et al. 2004), similarly to low-mass active stars at the same high activity levels (e.g., Sanz-Forcada et al. 2002; Testa et al. 2004); on

the other hand, there is evidence for significant differences such as much lower coronal filling factors (Testa et al. 2004), and very limited flaring activity. The evolved intermediate mass giants, both in the Hertzsprung gap and in the post helium flash "clump" (the relatively long-lived, $\sim$ 70 Myr, core Helium burning phase; Ayres et al. 1999), show extremely constant X-ray emission level (e.g., Haisch & Schmitt 1994; Gondoin 2003; Testa et al. 2004; Audard et al. 2004; Scelsi et al. 2004) and only a few flares have been observed on these sources (Haisch & Schmitt 1994; Ayres et al. 1999, and this work).

The opportunity of deriving a loop length from the analysis of the flare is interesting also in that it gives us an opportunity to probe the structuring of the corona, which in principle can be significantly different from dwarf stars coronae. In fact in these giants the gravity is considerably lower than for MS late-type stars therefore yielding a larger scale height, and possibly allowing the existence of very extended coronae (as suggested for example by Ayres et al. 2003). In the case of HR 9024 the surface gravity is only $\sim 0.02 g_{\odot}$ implying a scale height of about 3 stellar radii at 10^7 K ($30 R_{\star}$ at 10^8 K).

HR 9024 (HD 223460, OU And) is a moderately rotating ($v \sin i \sim 21$ km s^{-1}, de Medeiros & Lebre 1992) chromospherically active single giant, not too well studied even though it is a bright and close by object ($d \sim 135$ pc, Perryman et al. 1997). The stellar parameters are listed in Table 1. Several X-ray observations of HR 9024 exist indicating high and constant X-ray luminosity of a few 10^{31} erg s^{-1}. Singh et al. (1996) analyzed ROSAT PSPC observations of chromospherically active stars and derived an X-ray luminosity $L_{\rm X} \sim 4.3 \times 10^{31}$ erg s^{-1} in the $0.2-2.4$ keV energy band; this translates to $L_{\rm X} \sim 2.6 \times 10^{31}$ erg s^{-1} using the revised distance of 135 pc instead of 175 pc assumed by Singh et al. (1996). This value is in a good agreement with values obtained by Gondoin (2003), in the $0.3-2$ keV range, from two short XMM-*Newton* observations of HR 9024 showing little if any variability: $L_{\rm X} \sim 2.7 \times 10^{31}$ erg s^{-1} (Rev.107, 6 ks exposure time), and $L_{\rm X} \sim 2.3 \times 10^{31}$ erg s^{-1} (Rev.200, 3 ks exposure time); the total X-ray luminosities in the $0.3-10$ keV range are 3.8×10^{31} erg s^{-1} and 3.0×10^{31} erg s^{-1} respectively.

Table 1: Stellar parameters.

Spec. type	d [pc]	R [$R_{\odot}$]	M [$M_{\odot}$]	$\log L_{\rm bol}$ [erg s^{-1}]	$P_{\rm rot}$ [days]
G1 III	135[a]	13.6[b]	2.9[c]	35.4[d]	23.25[e]

References:(a) from SIMBAD; (b) Singh et al. (1996); (c) Gondoin (1999); (d) Flower (1996); (e) Singh et al. (1996).

Our approach here is to inspect the flare lightcurve and spectra and derive some quan-

tities relevant to set up a loop hydrodynamic model and to constrain the initial parameters. The numerical solution of the hydrodynamic equations allow us to synthesize in detail the emission (the so-called *forward modeling*) as it would be really observed and therefore to compare directly to the data. This allows us to have a feedback on the model and to refine the model parameters. Once obtained a good description of the global features, i.e. the lightcurve and the overall evolution of the temperature and total emission measure, the model will have constrained the loop length and aspect, and the heating function. The comparison with the fine details of the data analysis will give us insight into the flare density and thermal structure and evolution, and help us to interpret the results of the data analysis.

The paper is structured as follows: we describe the observations in §2, and the methods both for the spectral analysis and the hydrodynamic modeling in §3; in §4 we present the results of our study, and in §5 we draw our conclusions.

2. Observations

We analyzed the *Chandra* High Energy Transmission Grating Spectrometer (see Canizares et al. 2000, 2005 for a description of the instrumentation) observation of the X-ray active single G1 giant HR 9024. The data were obtained from the *Chandra* Data Archive[5] and have been reprocessed using standard CIAO 3.3 tools and analysis threads. Effective areas and line responses (ARFs and RMFs) were calculated using standard CIAO procedures[6]. The characteristics of the HETG observation are listed in Table 2.

Table 2: Parameters of HETG observation.

ObsID	Start	End	$t_{\rm exp}$ [ks]	$\log L_{\rm X}$[a] [erg s^{-1}]	$\log L_{{\rm X},peak}$[b] [erg s^{-1}]
1892	2001-08-11 00:19:04	2001-08-12 03:43:14	95.7	31.8	32.1

[a]From MEG spectrum, in the 2-24Å range. Averaged over the whole observation.

[a]Peak X-ray luminosity obtained from the MEG spectrum integrated in the time interval 10-15 ks from the beginning of the observation.

Figure 1 shows the *Chandra* High Energy (HEG) and Medium Energy (MEG) Gratings spectra for the $\sim$ 96 ks observation of HR 9024. The spectrum is characterized by a

[5]http://cxc.harvard.edu/cda

[6]see http://cxc.harvard.edu/ciao/threads/

strong continuum emission, indicating high temperature plasma, as well as the unusually strong Fe XXV complex at ~ 1.85Å ($\log T$[K] ~ 7.8), and Ca XX resonance line at 3.02Å ($\log T$[K] ~ 7.7); these characteristics are somewhat extreme when compared with the spectra of other very active stellar coronae (see e.g.,Testa et al. 2004). Other prominent features in the spectrum are the H-like and He-like lines of Si ($\sim 6.2, 6.7$Å respectively) and Mg ($\sim 8.4, 9.2$Å), and the strong emission lines of highly ionized Fe around 11Å.

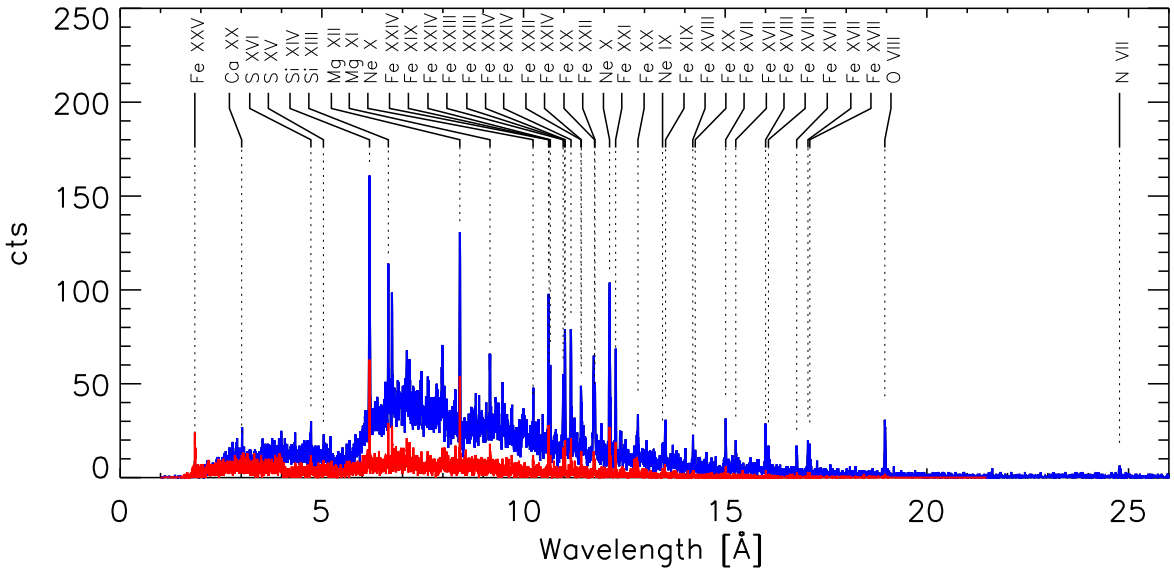

Fig. 1.— *Chandra* HEG (red) and MEG (blue) spectra obtained in a 96 ks observation of the single giant HR 9024. Line identification for many prominent spectral features is provided.

The lightcurve of the summed HEG+MEG dispersed photons integrated in the 1.5-26Å range, presented in Figure 2, shows clear variability: the X-ray emission level rises steeply at the beginning of the observation by a factor ~ 3 in about 15 ks; after a slow decay on a timescale of about 40 ks the lightcurve rises again, with peak around 80 ks from the beginning of the observation. The lightcurves for a hard (1.5-12Å) and a soft (12-26Å) spectral band, also shown in Fig. 2, indicate hardening of the spectrum corresponding to the two peaks of the emission, typical of stellar flares. The peak luminosity above 10^{32} erg s^{-1} is extremely high when compared with typical energies of stellar flares observed in active coronae of late-type stars.

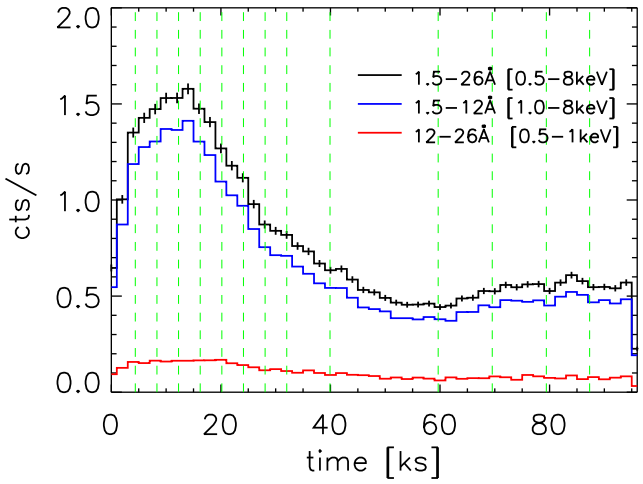

Fig. 2.— Lightcurve obtained as the sum of total counts of HEG and MEG dispersed spectra, using a temporal binsize of 2 ks. Lightcurves in hard (blue) and soft (red) spectral bands are shown. The vertical green dashed lines mark the time intervals selected for the temporally resolved spectral analysis and the hydrodynamic modeling (see §3).

3. Analysis

Spectra were analyzed with the PINTofALE[7] IDL[8] software (Kashyap & Drake 2000). The high resolution spectra provide several plasma diagnostics (temperature, density, abundances, emission measure distribution), from the analysis of both continuum and emission lines, and from the lightcurves in different spectral bands or in single lines. The high flux allows us to examine spectral line and continuum diagnostics at high temporal resolution.

3.1. Spectral analysis

Continuum emission: The strong continuum emission in this spectrum provides us with constraints on the hot plasma on which it strongly depends. Specifically, temperature and emission measure, EM, can be estimated through a fit of the continuum, and their evolution, probing the hottest plasma component, allows us to constrain the hydrodynamic model of the flaring structures (see §3.2, and §4.2). In order to derive T and EM, we fit the continuum

[7]http://hea-www.harvard.edu/PINTofALE

[8]Interactive Data Language, Research Systems Inc.

simultaneously in the HEG and MEG spectrum, selecting narrow spectral regions which can be assumed as "line-free" to a reasonable extent, on the basis of predictions of the atomic databases APED (Smith et al. 2001), and CHIANTI (Dere et al. 1997; Landi et al. 2006). We fit the continuum with an isothermal model computed in PINTofALE, using CHIANTI, and convolved with the HETG spectral response. This model contains all the contributions to the continuum (free-free, free-bound, 2 photon), however at high temperature ($\log T[\mathrm{K}] \gtrsim 7.5$), as observed in this spectrum, the bremsstrahlung continuum is by far the dominant process for the formation of the continuum. The "line-free" spectral regions used for the fit are: $2.00 - 2.95$Å, $4.4 - 4.6$Å, $5.3 - 6.0$Å, $7.5 - 7.8$Å, $12.5 - 12.7$Å, $19.1 - 20$Å. The fit also provides an estimate for EM from the normalization parameter. The analysis of the strong continuum emission allows us to derive the evolution of the temperature and emission measure during the flare with high temporal resolution. The time intervals chosen for this analysis are shown in Fig. 2 superimposed on the lightcurve; they have been selected in order to have high temporal resolution but also good constraints on the plasma parameters.

Line emission: The line fluxes are determined using the technique of spectral fitting described in Testa et al. (2004). The measured line fluxes have been used for the reconstruction of the emission measure distribution and the determination of abundances (§4.1), and for the comparison with the results of the hydrodynamic model (§4.2).

Abundances and Emission Measure Distribution: The emission measure distribution, EM(T), is derived through a Markov-Chain Monte-Carlo analysis using the Metropolis algorithm (MCMC[M]; Kashyap & Drake 1998) on a set of line flux ratios, as in García-Alvarez et al. (2006). O lines are the coolest lines used and Ar lines the hottest, covering a temperature range $\log T[\mathrm{K}] \sim 6.2 - 7.8$. Coronal abundances are evaluated on the basis of the derived EM(T): the abundance is a scaling factor in the line flux equation to match the measured flux (García-Alvarez et al. 2006).

3.2. Hydrodynamic modeling

The inspection of the light curve and of the evolution of the temperature and of the integrated emission measure (EM) during the flare allows to set up a detailed model of the flaring structure(s) (Reale et al. 2004), as described in detail in §4.2. We derive the temperature and EM parameters through the analysis of the continuum emission as described above (§3.1), the continuum emission being strong and probing the hottest plasma.

The 1D hydrodynamic model, solves time-dependent plasma equations with detailed energy balance (Peres et al. 1982; Betta et al. 1997), with a time-dependent heating function defining the energy release triggering the flare (see e.g., Reale et al. 1997, 2004). The coronal plasma is confined in a closed loop structure, where plasma motion and energy transport occur only along magnetic field lines. For the initial atmosphere we assume a loop in hydrostatic equilibrium and detailed energy balance (Serio et al. 1981) with maximum temperature (at the apex) $T_{\rm max} = 2 \times 10^7$ K; the initial conditions do not influence much the evolution of the plasma after a very short time.

The outputs of the hydrodynamic simulations are distributions of temperature and density along the loop sampled at regular times throughout the flare evolution. From these plasma parameters we synthesize the corresponding HETG spectrum of each (isothermal) plasma volume along the loop at each given time, using isothermal models folded with the HETG spectral response. We then integrate along the loop to obtain the overall HETG spectrum of the multi-thermal plasma in the flaring structure.

4. Results

4.1. Emission measure distribution and abundances

As a first step we carry out an analysis of the spectrum to study the global characteristics of thermal distribution and abundances. To obtain this information we need strong lines, from different elements, covering a wide temperature range. We have to integrate on time intervals long enough to have good photon statistics for each line. This limits our temporal resolution and we are not able to derive EM(T) and abundances in several portions of the flare, but only in two different portions of the observation: during the flare (i.e. using the spectrum integrated over the first 40 ks of the observation), and outside the flare (40-96 ks). We note that hereafter we will label the parameters derived outside the flare as "quiescent"; even though the corona seems to undergo another dynamic event this second flare is on a smaller scale with respect to the first one. The analysis of the abundances is useful also for the synthesis of the spectra from the results of hydrodynamic modeling and a consistent comparison with the data.

Table 3 lists the fluxes of the spectral lines used for this analysis, measured in the two phases of flare and quiescence.

Fig. 3 and 4 show the emission measure distribution and the coronal abundances as derived from the flare spectrum, and from the quiescent emission.

Table 3. Measured fluxes (in 10^{-6} photons cm^{-2} sec^{-1}) of the spectral lines used in our analysis, during the flare and outside the flare.

ion	$\lambda_{\rm obs}$ [Å]	$\log T_{\rm max}$[K][a]	flux$_{\rm flare}$	flux$_{\rm quiesc}$	Use[b]
Fe XXV	1.853	7.8	94 ± 19	13.5 ± 8.4	M
Fe XXV	1.864	7.8	49 ± 16	16.0 ± 8.4	M
Ca XX	3.024	7.7	21.7 ± 6.8	< 4.4	S
Ca XIX	3.187	7.4	18.7 ± 6.4	5.8 ± 3.7	S
Ar XVIII	3.734	7.6	14.1 ± 7.0	4.2 ± 3.6	S
Ar XVII	3.945	7.3	13.5 ± 6.7	4.7 ± 4.0	S
S XVI	4.729	7.4	20.3 ± 8.7	10.8 ± 5.7	S
S XV	5.041	7.2	30 ± 11	9.5 ± 6.0	S
Si XIV	6.183	7.2	82.9 ± 6.0	42.2 ± 3.6	SM
Si XIII	6.648	7.0	33.1 ± 4.2	25.7 ± 3.0	S
Al XIII	7.170	7.1	15.9 ± 4.5	8.1 ± 3.1	S
Al XII	7.759	6.9	6.2 ± 3.8	5.6 ± 3.1	S
Mg XII	8.422	7.0	80.7 ± 6.4	47.5 ± 4.5	SM
Mg XI	9.168	6.8	31.0 ± 4.7	15.2 ± 2.8	S
Ne X	12.132	6.8	142. ± 12.	113. ± 9.3	S
Fe XXI	12.284	7.0	79. ± 11.	53.5 ± 7.2	S
Ne IX	13.448	6.6	20. ± 10.	22.6 ± 7.4	S
Fe XVIII	14.201	6.9	50. ± 15.	30.1 ± 9.1	S
Fe XVII	15.012	6.7	107. ± 22.	43. ± 13.	S
O VIII	18.965	6.5	270. ± 42.	179. ± 29.	S
O VII	21.602	6.3	51 ± 44.	< 25	S
N VII	24.778	6.3	65. ± 50.	72. ± 40.	S

[a]Temperature of maximum formation of the line.

[b]Use indicates whether the line was used in the spectral analysis ("S"), for the emission measure reconstruction and abundance determination, and whether the feature was used for the direct comparison with the loop model ("M"; see §4.2).

The thermal distribution of the coronal plasma in HR 9024 appears dominated by hot (i.e., typical of flaring structures) plasma both during and outside the flare. Hot emission ($T \gtrsim 2 \times 10^7$ K) was found also from the analysis of two very short (6 ks, and 3 ks) XMM-*Newton* observations of HR 9024 when the corona seems to be in its quiescent state (Gondoin 2003). The main difference between the EM(T) of flare and quiescence is at the hot end of the temperature range, i.e. for $\log T[\mathrm{K}] \gtrsim 7.5$, where the EM(T) of the flaring plasma is about one order of magnitude higher than the EM(T) of the plasma outside the flare. The EM(T) derived for HR 9024 presents interesting characteristics when compared to other active coronae. Specifically, the EM(T) of HR 9024 is characterized by a rather shallow slope, similar to the slope of hydrostatic loop models ($EM(T) \propto T^{3/2}$; Rosner et al. 1978), whereas for several active coronae there is increasing evidence of steep, almost isothermal, emission measure distributions possibly indicating the dynamic nature of the coronal loops composing them (Testa et al. 2005b): for instance, such steep EM(T) are derived for other giants, e.g., the Hertzsprung gap giant 31 Com (Scelsi et al. 2004), and the clump giants β Cet, (Sanz-Forcada et al. 2002), and Capella (Dupree et al. 1993), and for other active stars (e.g., Griffiths & Jordan 1998; Drake et al. 2000; Sanz-Forcada et al. 2002).

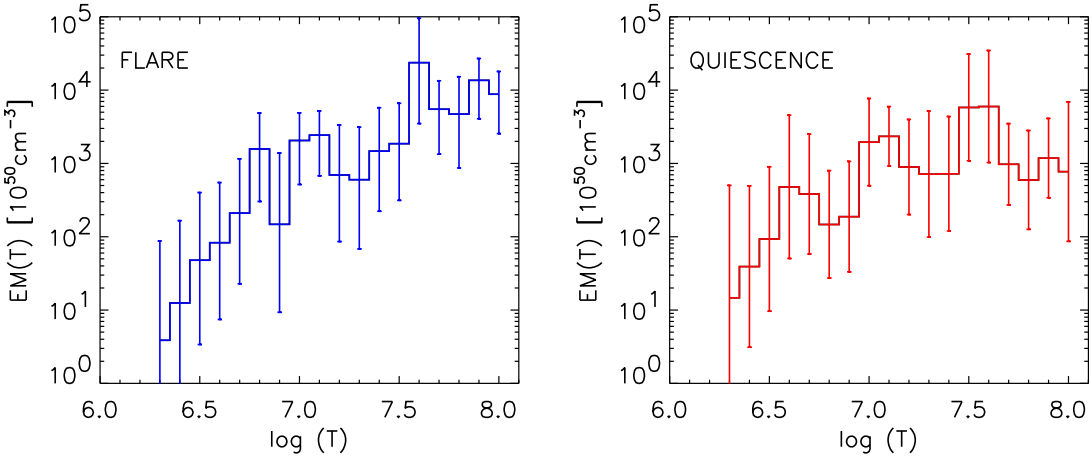

Fig. 3.— Emission measure distribution derived from the flare portion of the spectrum (0-40 ks; *left*), and from the spectrum outside the flare (40-96 ks; *right*). The comparison shows that the main difference between flare and quiescent emission resides in the hot end of the temperature range, i.e. for $\log T[\mathrm{K}] \gtrsim 7.5$ where the EM(T) of the flaring plasma is about one order of magnitude higher than the EM(T) of the plasma outside the flare.

The coronal abundance pattern observed in HR 9024 (Fig. 4) presents characteristics similar to other intermediate mass giants, i.e. little or no FIP effect (García-Alvarez et al. 2006). All abundances are plotted relative to the solar mixture of Asplund et al. (2005) as

photospheric abundances for HR 9024 have not been determined. We find significant changes in the coronal abundances during the flare with respect to the quiescent phase: all elements appear to be enhanced, except possibly Ne, and the Fe abundance in particular is found to increase by almost a factor 3.

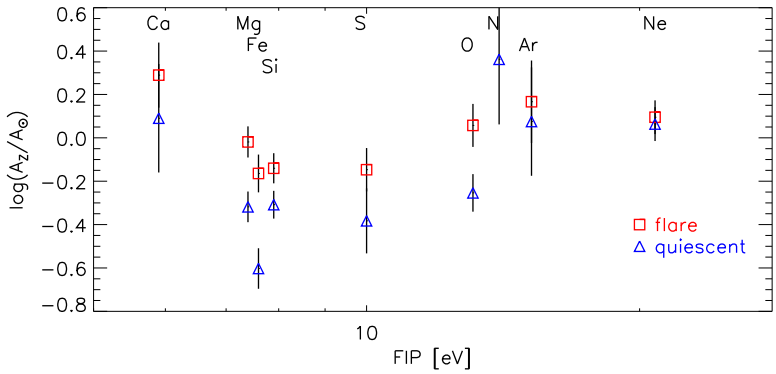

Fig. 4.— Coronal abundances relative to solar abundances (Asplund et al. 2005) as a function of the First Ionization Potential (FIP) derived for HR 9024 during the flare (square symbols) and the quiescent (triangles) phase.

Both abundances and EM(T) for HR 9024 have been derived also by Nordon & Behar (2006), and their findings are in agreement with the results presented here.

4.2. Flaring loop modeling

High level diagnostics of the flare can be obtained from detailed hydrodynamic modeling of the flaring plasma (Reale et al. 1988, 2004). The analogy of stellar to solar flares suggests that stellar as solar flares mainly occur in closed magnetic structures (coronal loops). It is customary to assume that the bulk of the flare involves a single coronal loop, which can be then investigated through the analysis of the flare characteristics.

The plasma confined in coronal loops can be described as a compressible fluid which moves and transports energy exclusively along the magnetic field lines. We can then model a flare by solving the time-dependent hydrodynamic equations in the coordinate along the loop with the assumption of an appropriate transient input heating function. The main model parameters include the loop length and the intensity, distribution and duration of the heat pulse. These parameters are constrained by the observed flare evolution, in particular in the decay phase, and by parameters derived from the data analysis, such as the temperature and emission measure at flare maximum and the timing of the maximum. Scaling laws such as

those shown in Reale et al. (1997) help us to constrain the loop length from the light curve decay time and the flare maximum temperature:

$$L_9 = \frac{\tau_X \sqrt{T_7}}{120 f(\zeta)} \tag{1}$$

where L_9 is the loop half length (10^9 cm), τ_X the decay time of the light curve, T_7 the flare temperature (10^7 K), $f(\zeta) \gtrsim 1$ a correction factor which takes into account possible significant heating during the decay, that might make the decay slower.

Other parameters, such as the loop initial atmosphere, or, for low gravity stars, the stellar surface gravity, have much less influence on the flare evolution. We compute the evolution of the loop plasma by solving the time-dependent hydrodynamic equation of mass, momentum and energy conservation for a compressible plasma confined in the loop (Peres et al. 1982; Betta et al. 1997), including the relevant physical effects such as the plasma thermal conduction and radiative losses. The gravity component along the loop is computed assuming a radius $R_* = 3R_\odot$ and a surface gravity $g_* = 0.1 g_\odot$.

We integrate numerically the equations over a time range of 50 ks. From the density and temperature distribution of the plasma along the model loop, we synthesize the expected plasma X-ray model spectrum, and finally convolve with the *Chandra*/MEG spectral response to produce synthetic counts spectra as described in §3.2.

The flare light curve integrated in the whole *Chandra*/MEG band resembles quite closely the X-ray light curves of flares recently observed on PMS stars (Favata et al. 2005). For this reason, we have assumed as a first set of parameters the same values which best describe a specific flare observed in the Orion region, i.e. a loop with constant cross-section and half-length $L = 10^{12}$ cm, symmetric around the loop apex. The flare simulation is triggered by injecting a heat pulse in the loop which is initially at a temperature of ~ 20 MK. Two heat pulses are deposited with a Gaussian spatial distribution of intensity 10 erg cm^{-3} s^{-1} and width 10^{10} cm (1/100 of the loop half-length) at a distance of 2×10^{10} cm from the footpoints, i.e. very close to them (Reale et al. 2004). After 20 ks the heat pulses are switched off completely. With the above parameters, the light curve is reproduced with good accuracy but we have noticed that the temperature values obtained from fitting the spectra with isothermal plasma emission models are significantly higher than those derived from the data all along the flare evolution (Testa et al. 2005a). Therefore, we have refined the model parameters to improve the fitting: we have reduced the input heating enough to account for the desired temperature decrease. From Eq.(1), in order to maintain the same decay time, a temperature reduction implies a shorter loop length. After this feedback, we have obtained best results with a loop half-length $L = 5 \times 10^{11}$ cm (half as before) and a heat pulse of

4 erg cm^{-3} s^{-1} (peak volumetric heating) lasting 15 ks (5 ks less than before). The total energy flux rate is 2.0×10^{11} erg cm^{-2} s^{-1}.

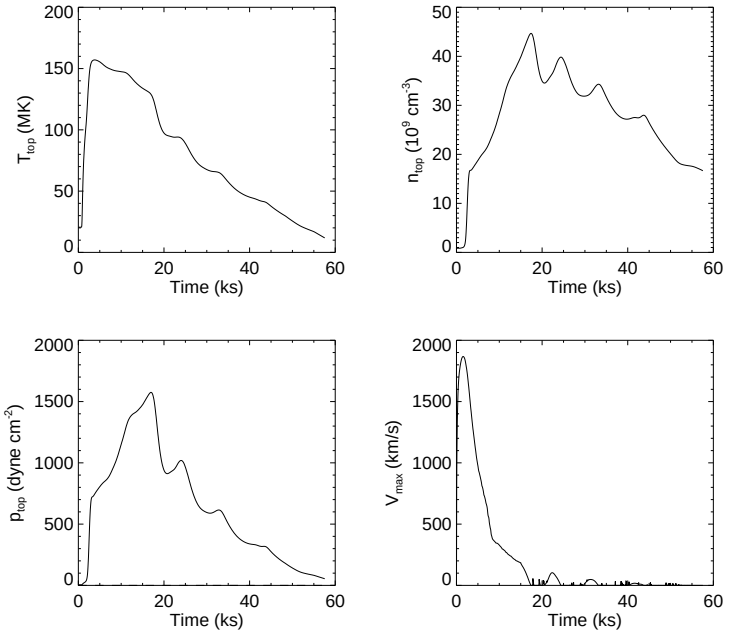

Fig. 5.— Evolution of the temperature, density and pressure at the loop apex and of the maximum plasma velocity according to the loop hydrodynamic model of the flare.

The computed evolution largely resembles the evolution computed for other stellar flares, although on larger scales than for typical flares observed in late-type stars coronae (e.g. Reale et al. 2004). Fig. 5 shows the evolution of the temperature, density, pressure at the apex of the loop and of the maximum plasma velocity. The heat pulses make the loop plasma heat rapidly ($\sim$ 3 ks) at temperatures about 150 MK and expand dynamically upward from the chromosphere at speeds about 1800 km s^{-1} to reach the loop apex also in about 3 ks. After this first impulsive phase, the temperature slowly decreases to about 130 MK while the heat pulse is on, and the evaporation of plasma from the chromosphere – which brings the density increase shown in Fig. 5 – continues substantially but less dynamically, with plasma speeds below 500 km s^{-1} after 9 ks, when the plasma pressure becomes higher than 1000 dyne cm^{-2}. The plasma pressure and density reach their peak of 1500 dyne cm^{-2} and 4.5×10^{10} cm^{-3} slightly (about 3 ks) later than the end of the heat pulse. Then they begin to decrease gradually with significant quasi-periodic fluctuations, while the temperature initially drops and then decreases more gradually.

Figure 6 shows the integrated light curve assuming a loop cross-section radius of 4.3×10^{10} cm, i.e. 8% of the loop half-length. The spectra obtained from the loop modeling have

also been fit with isothermal models. The resulting evolution of the emission measure and of the temperature, and the T vs. EM diagram are shown in the figure. A visual comparison of the model results with the data and the data fitting results indicates that the loop simulation results are in good agreement with the data.

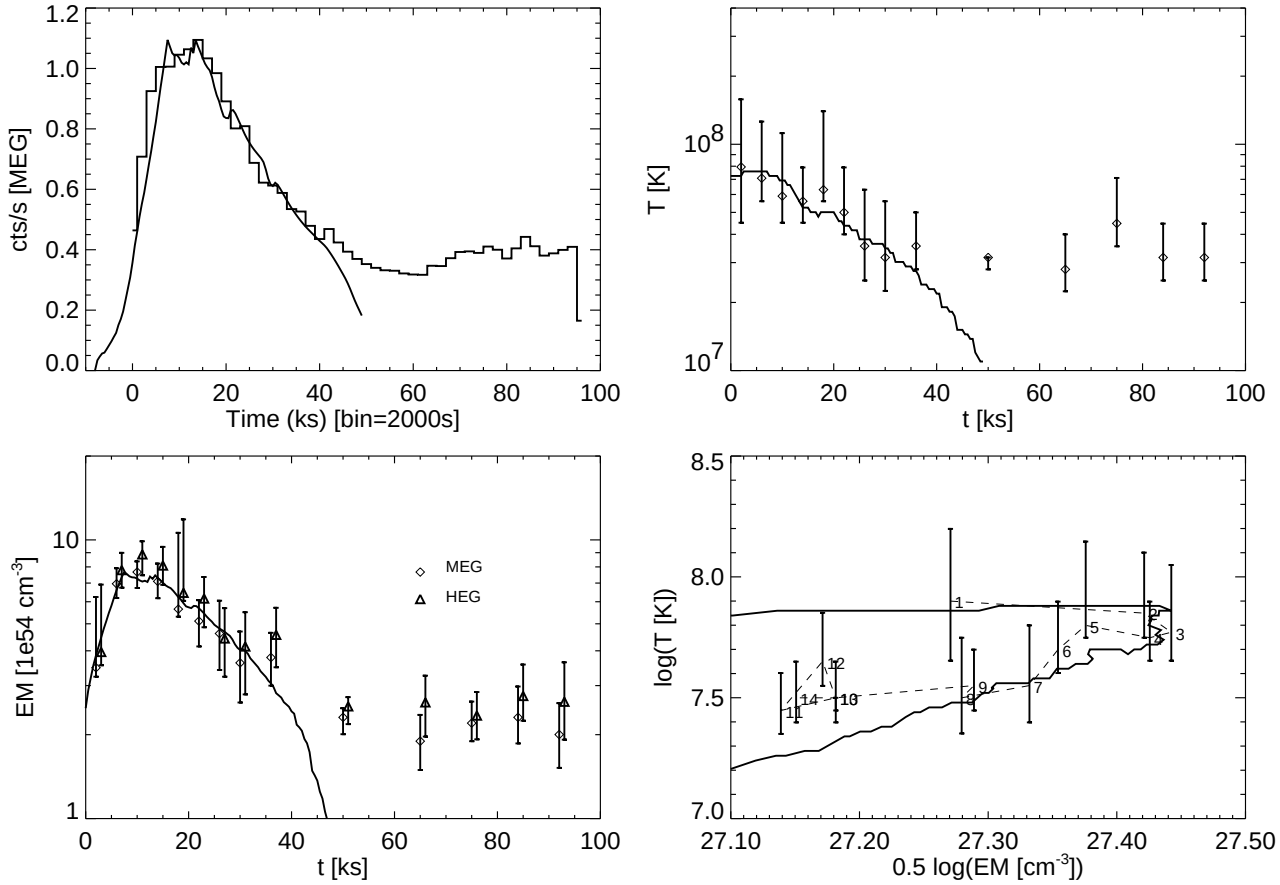

Fig. 6.— Comparison of observed lightcurve (top left), T (top right), EM (bottom left), and T-n (bottom right) evolution, with the corresponding quantities synthesized from the hydrodynamic loop model (solid thick lines) characterized by half-length $L = 5 \times 10^{11}$ cm, and footpoint impulsive heating. Evolution of temperature and emission measure (top right, and bottom left panels) are derived from the fit with isothermal models to the continuum emission in the spectra integrated in the time intervals shown in Fig. 2.

The dynamic model described above closely matches the evolution of temperature and emission measure derived from the continuum emission, and the lightcurve integrated over the entire wavelength range. The high quality data allows us to test the model and perform a detailed comparison of its characteristics with the observations. In Figure 7 we compare the MEG spectra synthesized from the model with the observed spectra in 4 different phases of

the flare: rise (0-10 ks from beginning of observation), peak (10-15 ks), early decay (15-30 ks), and late decay (30-45 ks). Figure 7 shows a general good agreement of the model spectra with the observations; however, some systematic discrepancies are observed. For example, in the spectrum of the late decay phase several lines, such as the Si XIV Lyα ($\sim$ 6.2Å), the hot Fe lines around 11Å, and the O VIII Lyα ($\sim 19\mathring{A}$), are overpredicted. There are several factors that may determine these departures from the observations. For instance, the abundances used for synthesizing the model spectrum are the ones derived from the flare spectrum and are kept fixed. Since we observe significant changes in the abundances after the flare (§4.1) they may change on short time scales and affect the emission in the spectral lines. Another process, not taken into account in our modeling, that might affect the emission in the lines on short time scale is non-equilibrium ionization; however, this effect is expected to be relevant only at the very beginning of the flare (see e.g., Orlando et al. 2003). Furthermore, in our simulation we assume that all the observed emission comes from the flaring structure, i.e. the emission of the quiescent corona (or of other secondary flaring structures) is assumed to be negligible whereas it could in fact contribute significantly to the "cool" ($\log T[\mathrm{K}] \lesssim 7.2$) lines at least, as suggested by the derived emission measures during flare and quiescence (Fig. 3).

The high quality of the data allows us to test the model to a much higher level of detail than before, for instance allowing a direct comparison with the lightcurves in single spectral features. The evolution in very hot spectral features emitted at the bulk plasma temperature of the flaring loop (i.e. $\log T[\mathrm{K}] > 7.5$) would represent more meaningful tests for the model. However, there are only a few very hot lines present in the spectrum (e.g., Fe XXV and Ca XX), and only the Fe XXV complex has enough signal to provide temporal resolution. Beside Fe XXV, we selected two other emission lines with high enough flux, Si XIV and Mg XII Lyα lines, and derived their lightcurves using the same time intervals used for the analysis of the continuum and marked in Fig. 2. Figure 8 compares the lightcurves in these spectral features derived from the observations with those synthesized from the hydrodynamic simulation, assuming a loop cross-section radius $r = 4.8 \times 10^{10}$ cm. The line fluxes for Si XIV and Mg XII are obtained from the fit to the spectra integrated in each time interval. For the Fe XXV complex the lower signal to noise ratio does not constrain the fit; however, since in the relevant wavelength range the continuum emission is rather small with respect to the line emission we use the lightcurve integrated in a small wavelength range (1.83-1.89Å) using a 3 ks temporal bin.

The model reproduces extremely well the observed temporal behaviour of the Fe XXV line complex. The lightcurves of Si XIV and Mg XII derived from the observation and from the model lie close to each other up to the peak of the flare. After the peak the observed emission in the two lines experiences the dramatic drop predicted from the model, but on

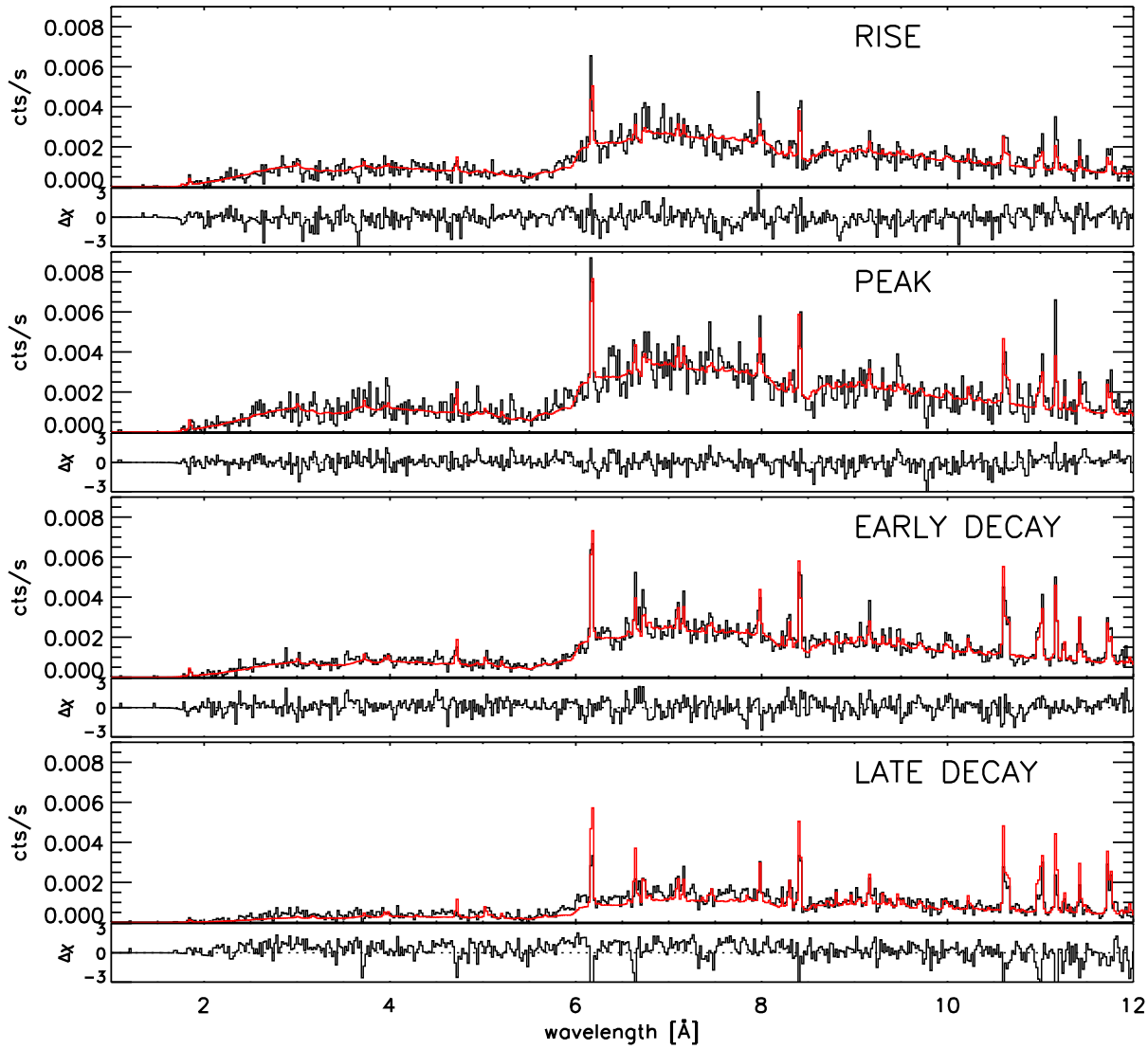

Fig. 7.— Comparison of HR 9024 MEG spectrum (black histogram) and the MEG spectrum synthesized from the hydrodynamic model (red histogram) in four different phases of the flare, from top to bottom,: rise (0-10 ks from beginning of observation), peak (10-15 ks), early decay (15-30 ks), and late decay (30-45 ks). Spectra are shown in counts per second, and for better readability we split the spectral range in two plots showing the spectral range 1.5-12Å and 12-22Å respectively. The small panel below each plot shows the χ residuals.

much shorter timescales, anticipating the model by slightly more than 10 ks. Other than the effects discussed above possibly causing this discrepancy, we can identify another effect that may play a role. In the model of the flaring loop the plasma contributing the most to these "cool" lines ($\log T[\mathrm{K}] \sim 7.0 - 7.2$) is located in the transition region of the loop, that is the

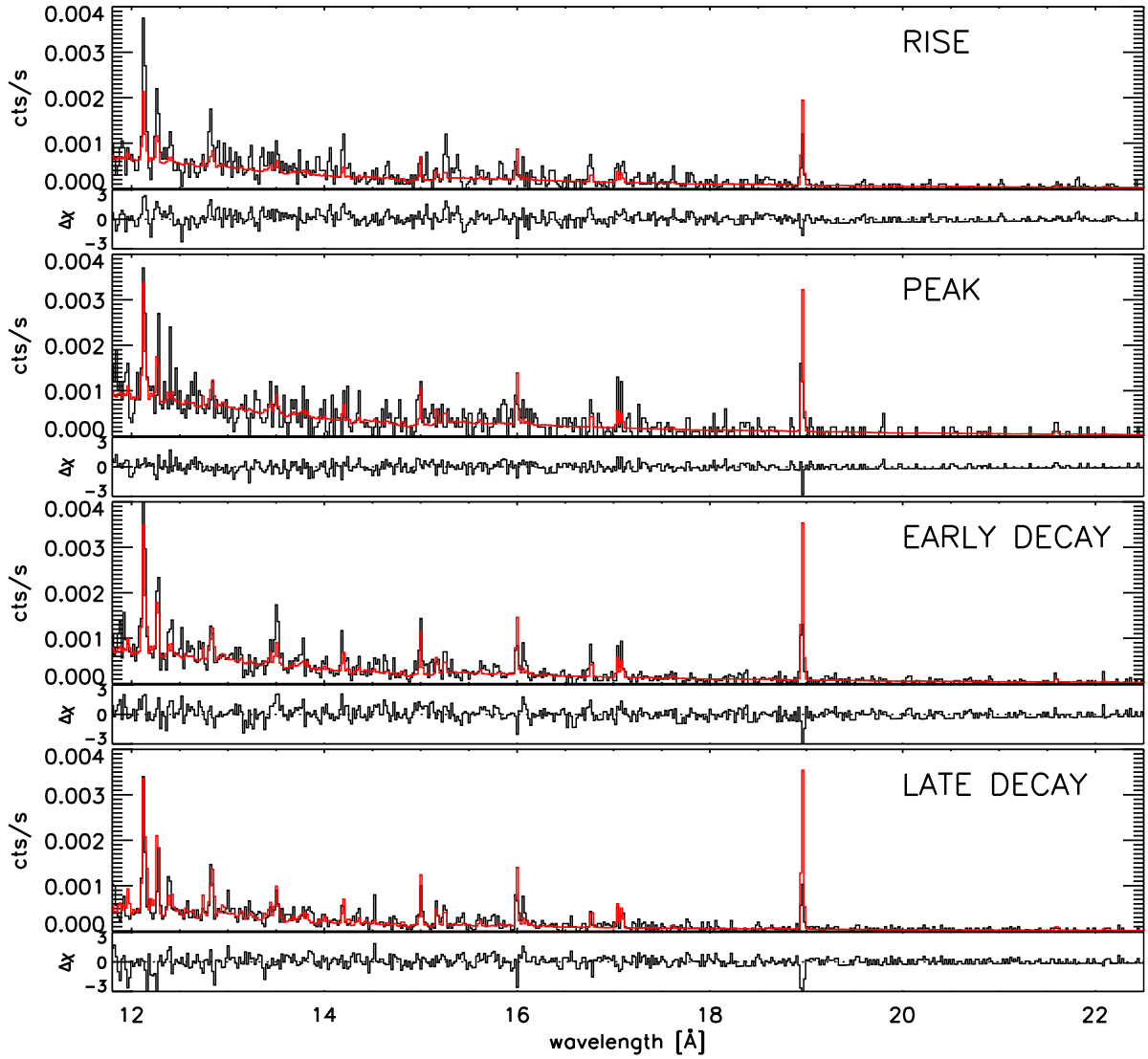

Fig. 7.— continued.

region where the plasma temperature and density steeply change from the dense and cool chromosphere to the hot and rarefied coronal portion of the loop. In this region some models predict an opening of the magnetic flux tube which could have a substantially larger cross-section in corona than in the low region connecting it to the photosphere (e.g., Gabriel 1976; Schrijver et al. 1989; Litwin & Rosner 1993; Ciaravella et al. 1996). In this possible scenario, the emission of the flaring structure in these cool lines would be substantially reduced and the resulting excess would be therefore attributed to the background corona or to nearby secondary flaring structures (e.g., Betta et al. 2001).

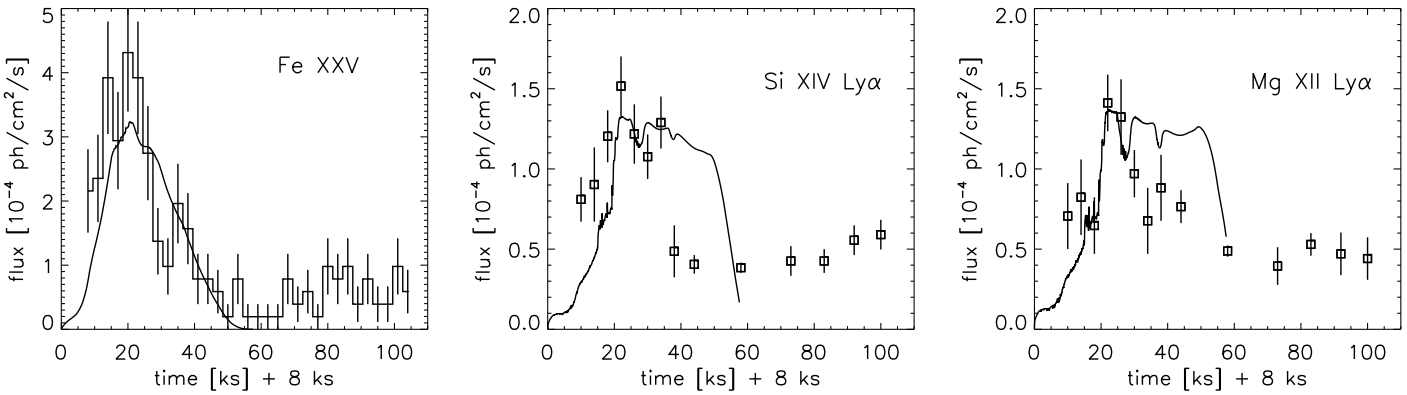

Fig. 8.— Lightcurves derived from HETG spectra in selected spectral features (histograms with error bars) compared with the prediction from the hydrodynamic model (thick solid line), assuming a loop cross-section radius 4.8×10^{10} cm.

Finally, we compared the emission measure distribution of the loop model with the EM(T) derived from the flare spectrum. Figure 9 shows that also for the emission measure distribution the model predictions are in very good agreement with the observations. This agreement is a further indication of the validity of the single loop model for this flare and, on the other hand, of the EM inversion method. In our modeling of the X-ray emission during the flare we assume any persistent quiescent emission to be negligible. As mentioned in §4.1, the *Chandra* observation does not provide a good determination of the quiescent emission as outside the large flare constituting the focus of our analysis the corona is undergoing another significant, though smaller, dynamic event (its average $L_{\rm X} \sim 4.2 \times 10^{31}$ erg s^{-1} is about twice the luminosity value of other X-ray observations; see §1 and §5). Other X-ray observations of this corona suggest that the quiescent emission is in fact negligible to a large extent with respect to the large and hot flare observed with *Chandra* (see §5).

5. Discussion and conclusions

Our analysis has shown that the observed evolution of the very hot coronal emission of the single giant HR 9024 is reproduced extremely well by a model characterized by loop semi-length $L = 5 \times 10^{11}$ cm ($\sim R_\star/2$), and impulsive footpoint heating triggering the flare. The heating pulse lasts 15 ks, and it is shifted by 8 ks preceding the beginning of observation. The peak volumetric heating is 4 erg cm^{-3} s^{-1}, with a corresponding total heating rate $\approx 10^{33}$ erg s^{-1}. The detailed analysis of the plasma evolution in the temperature-density diagram (Fig. 6) put tight constraints on the flare morphology and on the characteristics

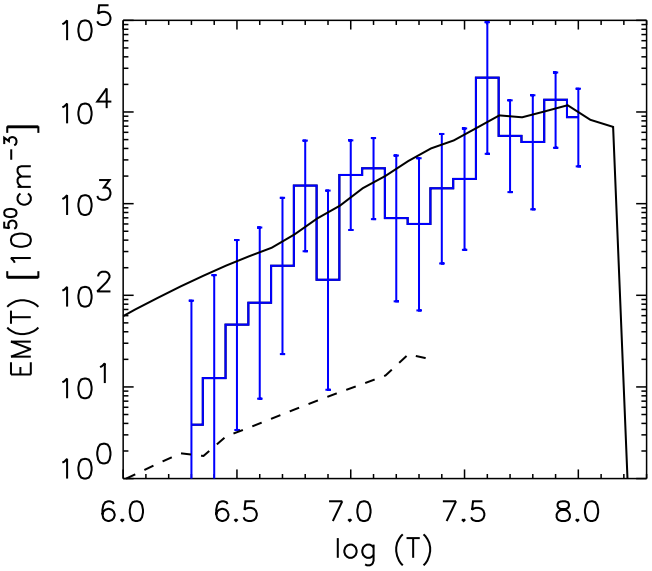

Fig. 9.— Comparison of emission measure distribution derived from the flare spectrum (histogram with error bars) with the EM(T) of the hydrodynamic loop model (solid thick line). The dashed line shows the EM(T) of the initial static loop with maximum temperature of 20 MK.

of the heating. The delay of the EM peak with respect to the temperature peak indicates that the X-ray emitting plasma is confined in a closed structure, whereas in non-confined coronal flares the EM evolves simultaneously with the temperature as shown by the analysis of hydrodynamic models (Reale et al. 2002). The steep slope of the decay path in the temperature-density diagram implies that after the initial phase when the energy is released, the loop undergoes a pure cooling evolution, and no addition heating is needed to explain the evolution of the flaring plasma.

As discussed in §4.2 the initial phases of the flare are very dynamic and the plasma fills up the loop expanding upward at very high speed reaching $\sim$ 1800 km s^{-1}. After about $\sim$ 10 ks, therefore corresponding to the start of the *Chandra* observation (considering the shift of 8 ks between the energy release and the start of the observation), the plasma speed rapidly decreases; however, during the first 5-10 ks of the observation plasma flows with speed up to a few 100 km s^{-1} are present. Such speed can be in principle resolved by HETG. The plasma characterized by such high speed is plasma at temperatures above 60 MK, therefore, in order to investigate these speeds through Doppler shifts we have to search for shifts in very hot lines. However, such hot lines, e.g. Ca XX, are at low λ where the effective area is low and the instrument is not very sensitive. We searched for shifts in

the Ca XX line but we did not detect any significant shift. We note that, even in the case the instrument sensitivity were not a limiting factor, the detection of line shifts is expected only for a preferential orientation of the loop with respect to the line of sight.

The high photon statistics of the HETG data allowed us to derive light curves in a few relevant hot lines and, for the first time for a stellar flare, they could be compared in detail to those predicted by a hydrodynamic model (see Peres et al. 1987; Betta et al. 2001, for analogous comparisons for a solar flare).

To a more general level, we could also compare the distributions of emission measure obtained from the data analysis and from the flare loop model and found a good agreement. The shape of the EM distribution is quite typical of a single coronal loop (e.g., Peres et al. 2000) and different from those found for active stars (e.g., Sanz-Forcada et al. 2002; Testa et al. 2005b; Cargill & Klimchuk 2006).

From the normalization of the model lightcurves we derive an estimate of the loop cross-section and therefore of its aspect ratio $\alpha = r/L$. We note that the loop cross-section radius, r, is a free parameter for which we can obtain independent estimates from the normalization of the different lightcurves: (a) integrated MEG dispersed counts, (b) EM derived from the analysis of the continuum (Fig. 6), and (c) fluxes of spectral features (Fig. 8), therefore providing a cross-check of the consistency of our model. The obtained values of $r = 4.9 \times 10^{10}$ cm, 4.3×10^{10} cm, and 4.8×10^{10} cm respectively, all agree within 15%, and they imply a loop aspect ratio $\alpha \sim 0.09$. Figure 10 shows a sketch of the morphology of the flaring structure as inferred from our modeling of the observed *Chandra*-HETG spectra.

As mentioned in §4.2, the loop model reproducing the observation has roughly the same parameters of models satisfyingly reproducing other large flares, specifically the flares observed in pre-main sequence stars (Favata et al. 2005). However, the derived loop parameters reveal some dissimilarity possibly indicating fundamental differences between the processes at work in the two cases. The flaring loop reproducing the flare on HR 9024 is characterized by loop semi-length $L \sim R_\star/2$, and aspect ratio $r/L \sim 0.1$, as typically found for low mass stars and on the Sun. In contrast, the modeling of the flare on the pre-main sequence stars, in particular the detailed model for COUP source 1343, yields a very large loop semi-length corresponding to several stellar radii, and with a much smaller aspect ratio $r/L \sim 0.02$ (Favata et al. 2005). These findings suggest that HR 9024 is characterized by a "normal" corona, while in the young stars showing evidence of elongated X-ray emitting structures, possibly connecting the star to the disk, processes profoundly different may be at work.

Large flares as the one observed in HR 9024 are very unusual in single intermediate mass giants, and there are only a few such events studied in detail. This study thus allowed

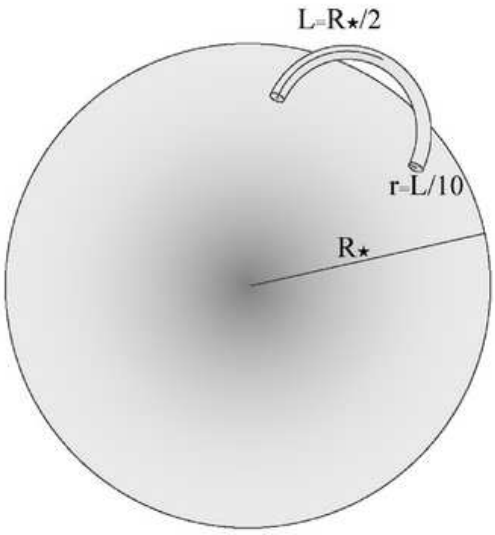

Fig. 10.— Sketch showing the geometry of the flaring loop of HR 9024 as derived from the hydrodynamic modeling of the flare: $R_\star$ is the stellar radius, L is the loop semi-length, and r is the cross-section radius of the loop.

us to investigate the flaring activity in a single giant, and provided us with a powerful tool to derive the size of its coronal structures. Even though the flaring structure modeled here is not necessarily representative of the typical coronal structures in X-ray active giants, as discussed above, its characteristics are consistent with the presence of a corona with properties typical of active coronae but scaled up to the larger stellar radius. The coronal properties derived through X-ray observations of these active giants might suggest a possible interpretation for the low frequency of flares. There is some evidence of very low coronal surface filling factors ($\lesssim 10^{-4}$) for these active giants as suggested from density analysis (e.g., Testa et al. 2004). Considering the interaction of magnetic fields in active regions as a possible mechanism increasing the X-ray flaring activity in active stars (Güdel et al. 1997; Testa et al. 2004), in these stars this kind of interaction might be much less frequent given to the very sparse presence of active region distributed on a large area.

In this paper both for the modeling and its interpretation we have assumed that the quiescent emission is negligible with respect to the flaring emission. The *Chandra* observation does not provide a good grasp of the quiescent emission as the hardness ratio behaviour (and the emission measure distribution) suggests the presence of another dynamic event subsequent to the large flare (as in Reale et al. 2004). The XMM-*Newton* observations might represent the quiescent X-ray spectrum of HR 9024 not showing significant variability, however their very low exposure time (6 ks, 3 ks) allow us only to assess the variability on very short time scales. Our preliminary results of a ~ 50 ks new Suzaku observation of HR 9024

shows extremely constant X-ray emission and provides an estimate of the quiescent X-ray luminosity and temperature of about 2×10^{31} erg s^{-1} and 3×10^{7} K respectively (P.Testa et al. in prep.), consistent with the findings based on XMM-*Newton* and ROSAT observations (Gondoin 2003; Singh et al. 1996). This X-ray luminosity value which we assume being a good estimate for the quiescent emission of HR 9024, is about an order of magnitude lower than the peak luminosity of the flare observed with *Chandra*, therefore lending support to the assumption that the quiescent emission is negligible with respect to the flare emission. Also, the main results of our study rely on the emission of the very hot plasma which is completely dominated by the flaring structure, and therefore they should not be significantly affected by ignoring the much cooler quiescent emission.

In this work we model the flare emission with a single loop structure and it is worth discussing whether and to what extent very different solutions can be ruled out. We model the bulk of the flare where presumably there is one dominant loop structure, as observed in many solar compact flares entirely occurring in single loops and even in more complex flares, where one can often consider a dominant loop (e.g. Aschwanden & Alexander 2001). The single loop model satisfactorily reproduces the *Chandra* observations analyzed in this work and multiple loop models would not add insight and would include more free and unconstrained parameters. Furthermore, the single loop model is supported by the fact that : (1) the loop cross-section area is consistent with that of a single loop structure; (2) the thermal distribution is compatible with that of a single flaring loop; (3) the decay path in the density-temperature diagram has quite a steep slope (~ 2) implying negligible heating in the decay (Sylwester et al. 1993), in turn indicating a single loop structure, whereas flaring arcades are characterized by significant heating (e.g. Kopp & Poletto 1984). At later times of our observation (when the light curve rises again) other loops may be involved and become important in the evolution (e.g. Reale et al. 2004). The general expression of the loop length as a function of the observed decay time (Eq. 1) also allows us to estimate the uncertainties on the derived loop length. In particular, using the expression of the correction factor $f(\zeta)$ tuned for Chandra, as reported in Favata et al. (2005), we obtain $L_9 = 490$. Considering typical uncertainties of the diagnostic formula, and the uncertainties on the observed temperature, we estimate an error of about 20-30% on the loop length, therefore yielding $L = 4.9 \pm 1.5 \times 10^{11}$ cm. It is worth noting that this formula used for estimating the uncertainties on the derived loop geometry assumes uniform heating and provides only approximate values for the loop length. The hydrodynamic model provides us with a much higher level of detail, giving us diagnostics for the temporal and spatial distribution of the heating, for the loop aspect, and for the thermal distribution of the plasma.

PT and DPH were supported by SAO contract SV3-73016 to MIT for support of CXC,

which is operated by SAO for and on behalf of NASA under contract NAS8-03060. FR acknowledges support from Agenzia Spaziale Italiana and italian Ministero dell'Università e della Ricerca.

REFERENCES

Aschwanden, M. J., & Alexander, D. 2001, Sol. Phys., 204, 91

Asplund, M., Grevesse, N., & Sauval, A. J. 2005, in ASP Conf. Ser. 336: Cosmic Abundances as Records of Stellar Evolution and Nucleosynthesis, ed. T. G. Barnes, III & F. N. Bash, 25–+

Audard, M., Telleschi, A., Güdel, M., Skinner, S. L., Pallavicini, R., & Mitra-Kraev, U. 2004, ApJ, 617, 531

Ayres, T. R., Brown, A., Harper, G. M., Osten, R. A., Linsky, J. L., Wood, B. E., & Redfield, S. 2003, ApJ, 583, 963

Ayres, T. R., Osten, R. A., & Brown, A. 1999, ApJ, 526, 445

Ayres, T. R., Simon, T., Stern, R. A., Drake, S. A., Wood, B. E., & Brown, A. 1998, ApJ, 496, 428

Betta, R., Peres, G., Reale, R., & Serio, S. 1997, A&AS, 122, 585

Betta, R. M., Peres, G., Reale, F., & Serio, S. 2001, A&A, 380, 341

Canizares, C. R., Davis, J. E., Dewey, D., Flanagan, K. A., Galton, E. B., Huenemoerder, D. P., Ishibashi, K., Markert, T. H., Marshall, H. L., McGuirk, M., Schattenburg, M. L., Schulz, N. S., Smith, H. I., & Wise, M. 2005, PASP, 117, 1144

Canizares, C. R., Huenemoerder, D. P., Davis, D. S., Dewey, D., Flanagan, K. A., Houck, J., Markert, T. H., Marshall, H. L., Schattenburg, M. L., Schulz, N. S., Wise, M., Drake, J. J., & Brickhouse, N. S. 2000, ApJ, 539, L41

Cargill, P. J., & Klimchuk, J. A. 2006, ApJ, 643, 438

Ciaravella, A., Peres, G., Maggio, A., & Serio, S. 1996, A&A, 306, 553

de Medeiros, J. R., & Lebre, A. 1992, A&A, 264, L21

Dere, K. P., Landi, E., Mason, H. E., Monsignori Fossi, B. C., & Young, P. R. 1997, A&AS, 125, 149

Drake, J. J., Peres, G., Orlando, S., Laming, J. M., & Maggio, A. 2000, ApJ, 545, 1074

Dupree, A. K., Brickhouse, N. S., Doschek, G. A., Green, J. C., & Raymond, J. C. 1993, ApJ, 418, L41+

Favata, F., Flaccomio, E., Reale, F., Micela, G., Sciortino, S., Shang, H., Stassun, K. G., & Feigelson, E. D. 2005, ApJS, 160, 469

Favata, F., Micela, G., Reale, F., Sciortino, S., & Schmitt, J. H. M. M. 2000, A&A, 362, 628

Flower, P. J. 1996, ApJ, 469, 355

Güdel, M., Guinan, E. F., & Skinner, S. L. 1997, ApJ, 483, 947

Gabriel, A. H. 1976, Royal Society of London Philosophical Transactions Series A, 281, 339

García-Alvarez, D., Drake, J. J., Ball, B., Lin, L., & Kashyap, V. L. 2006, ApJ, 638, 1028

Gondoin, P. 1999, A&A, 352, 217

—. 2003, A&A, 409, 263

Griffiths, N. W., & Jordan, C. 1998, ApJ, 497, 883

Haisch, B., & Schmitt, J. H. M. M. 1994, ApJ, 426, 716

Kashyap, V., & Drake, J. J. 1998, ApJ, 503, 450

—. 2000, Bulletin of the Astronomical Society of India, 28, 475

Kopp, R. A., & Poletto, G. 1984, Sol. Phys., 93, 351

Landi, E., Del Zanna, G., Young, P. R., Dere, K. P., Mason, H. E., & Landini, M. 2006, ApJS, 162, 261

Litwin, C., & Rosner, R. 1993, ApJ, 412, 375

Ness, J.-U., Güdel, M., Schmitt, J. H. M. M., Audard, M., & Telleschi, A. 2004, A&A, 427, 667

Nordon, R., & Behar, E. 2006, ArXiv Astrophysics e-prints

Orlando, S., Peres, G., Reale, F., Rosner, R., & Siegel, A. 2003, Memorie della Societa Astronomica Italiana, 74, 643

Osten, R. A., Drake, S., Tueller, J., Cummings, J., Perri, M., Moretti, A., & Covino, S. 2006, ArXiv Astrophysics e-prints

Peres, G., Orlando, S., Reale, F., Rosner, R., & Hudson, H. 2000, ApJ, 528, 537

Peres, G., Reale, F., Serio, S., & Pallavicini, R. 1987, ApJ, 312, 895

Peres, G., Serio, S., Vaiana, G. S., & Rosner, R. 1982, ApJ, 252, 791

Perryman, M. A. C., Lindegren, L., Kovalevsky, J., Hoeg, E., Bastian, U., Bernacca, P. L., Crézé, M., Donati, F., Grenon, M., van Leeuwen, F., van der Marel, H., Mignard, F., Murray, C. A., Le Poole, R. S., Schrijver, H., Turon, C., Arenou, F., Froeschlé, M., & Petersen, C. S. 1997, A&A, 323, L49

Pizzolato, N., Maggio, A., & Sciortino, S. 2000, A&A, 361, 614

Reale, F. 2002, in ASP Conf. Ser. 277: Stellar Coronae in the Chandra and XMM-NEWTON Era, 103

Reale, F., Betta, R., Peres, G., Serio, S., & McTiernan, J. 1997, A&A, 325, 782

Reale, F., Bocchino, F., & Peres, G. 2002, A&A, 383, 952

Reale, F., Güdel, M., Peres, G., & Audard, M. 2004, A&A, 416, 733

Reale, F., Peres, G., Serio, S., Rosner, R., & Schmitt, J. H. M. M. 1988, ApJ, 328, 256

Rosner, R., Tucker, W. H., & Vaiana, G. S. 1978, ApJ, 220, 643

Sanz-Forcada, J., Brickhouse, N. S., & Dupree, A. K. 2002, ApJ, 570, 799

Scelsi, L., Maggio, A., Peres, G., & Gondoin, P. 2004, A&A, 413, 643

Schmitt, J. H. M. M., & Favata, F. 1999, Nature, 401, 44

Schrijver, C. J., Lemen, J. R., & Mewe, R. 1989, ApJ, 341, 484

Serio, S., Peres, G., Vaiana, G. S., Golub, L., & Rosner, R. 1981, ApJ, 243, 288

Singh, K. P., Drake, S. A., White, N. E., & Simon, T. 1996, AJ, 112, 221

Smith, R. K., Brickhouse, N. S., Liedahl, D. A., & Raymond, J. C. 2001, ApJ, 556, L91

Sylwester, B., Sylwester, J., Serio, S., Reale, F., Bentley, R. D., & Fludra, A. 1993, A&A, 267, 586

Testa, P., Drake, J., & Peres, G. 2004, ApJ, 617, 508

Testa, P., Garcia-Alvarez, D., Reale, F., & Huenemoerder, D. 2005a, ArXiv Astrophysics e-prints

Testa, P., Peres, G., & Reale, F. 2005b, ApJ, 622, 695

Vaiana, G. S., Fabbiano, G., Giacconi, R., Golub, L., Gorenstein, P., Harnden, F. R., Cassinelli, J. P., Haisch, B. M., Johnson, H. M., Linsky, J. L., Maxson, C. W., Mewe, R., Rosner, R., Seward, F., Topka, K., & Zwaan, C. 1981, ApJ, 245, 163